

Electronic Supplementary Information

A Facile and Controllable, Deep Eutectic Solvent Aided Strategy for Synthesis Graphene Encapsulated Metal Phosphides for Enhanced Electrocatalysis Overall Water Splitting

Hongyu Mou,^[a]# Jinfang Wang,^[a]# Dongkun Yu,^[a]# Deliang Zhang,^[b]# Fu Lu,^[c] Lei Chen,^[b] Debao Wang,^[b] and Tiancheng Mu*^[a]

^[a] Department of Chemistry, Renmin University of China, No 59 Zhongguancun Street, Beijing 100872, China. E-mail: tcmu@ruc.edu.cn

^[b] Shandong Key Laboratory of Biochemical Analysis, College of Chemistry and Molecular Engineering, Qingdao University of Science and Technology, Qingdao 266042, China.

^[c] College of Materials Science and Engineering, Qingdao University of Science and Technology, Qingdao 266042, China.

These authors contributed equally to this work.

Table of the contents

1. Experiment Section
2. Supplementary Figures and Discussion
3. Supplementary Tables
4. References

1. Experiment Section

Materials.

$\text{NiCl}_2 \cdot 6\text{H}_2\text{O}$, $\text{CuCl}_2 \cdot 2\text{H}_2\text{O}$, $\text{FeCl}_2 \cdot 6\text{H}_2\text{O}$, $\text{CoCl}_2 \cdot 6\text{H}_2\text{O}$, KOH, $\text{NaH}_2\text{PO}_2 \cdot \text{H}_2\text{O}$, malonic acid, oxalic acid, succinic acid, and glutaric acid were purchase from Macklin, Pt/C (20 wt %) and IrO_2 were purchase from Alfa Aesar, and all other chemical materials were purchase from Sigma-Aldrich without further purification.

Preparation of $\text{Ni}_2\text{P}@$ graphene composites.

The $\text{Ni}_2\text{P}@$ graphene composites were prepared by a solution processing, followed by pyrolytic of deep eutectic solvents yield $\text{Ni}_2\text{P}@$ graphene composites. The detailed steps are as follows: First, 0.01 mol $\text{NiCl}_2 \cdot 6\text{H}_2\text{O}$ and 0.07 mol malonic acid were mixed well and placed in an oil bath at $90\text{ }^\circ\text{C}$, and stirred to form DES. Subsequently, the resulting DES was placed at the center of a tube furnace, and 2.0 g of $\text{NaH}_2\text{PO}_2 \cdot \text{H}_2\text{O}$ was placed at the upstream side and near to DES. After it was flushed with N_2 gas, the center of the furnace was elevated to the reaction temperature of $400\text{ }^\circ\text{C}$ with a ramping rate of $5\text{ }^\circ\text{C min}^{-1}$ and kept at $400\text{ }^\circ\text{C}$ for 4 h to convert the DES to $\text{Ni}_2\text{P}@$ graphene. As the furnace cooled, the $\text{Ni}_2\text{P}@$ graphene composites were obtained. By changing the amount of malonic acid used to regulate the loading of graphene, the amount of malonic acid in the experiment were 0.03 mol, 0.05 mol, 0.07 mol, and 0.09 mol for the preparation of DES-1, DES-2, DES-3, and DES-4, the corresponding phosphating and pyrolysis products are labeled as $\text{Ni}_2\text{P}@$ G-1, $\text{Ni}_2\text{P}@$ G-2, $\text{Ni}_2\text{P}@$ G-3, and $\text{Ni}_2\text{P}@$ G-4 respectively. In addition, $\text{Ni}_2\text{P}@$ graphene composites were prepared by changing the carbon precursor (oxalic acid, succinic acid, or glutaric acid).

Preparation of phosphide@graphene composites.

The phosphide@graphene composites were prepared by a solution processing, followed by pyrolytic of deep eutectic solvents yield phosphide@graphene composites. The detailed steps are as follows: First, 0.01 mol $\text{CuCl}_2 \cdot 2\text{H}_2\text{O}$, $\text{FeCl}_2 \cdot 6\text{H}_2\text{O}$, or $\text{CoCl}_2 \cdot 6\text{H}_2\text{O}$, and 0.07 mol malonic acid were mixed well and placed in an oil bath at $70\text{-}120\text{ }^\circ\text{C}$, and stirred to form a uniform liquid. The resulting liquid and $\text{NaH}_2\text{PO}_2 \cdot \text{H}_2\text{O}$ were heated in a tube furnace under nitrogen atmosphere at $400\text{ }^\circ\text{C}$ and held for 4 hours. As the furnace cooled, the metal phosphide@graphene composites were obtained.

Electrochemical measurements.

HER polarization curve tests were conducted on a 3000 potentiostat/galvanostat with a three-electrode electrochemical cell. Graphite rod was used as the counter electrode and Ag/AgCl (saturated KCl filled) as the reference electrode. A carbon cloth electrode with an area of $1 \times 1 \text{ cm}^2$ used as the working electrode. Typically, 20 mg catalyst was suspended in 0.5 mL deionized water, 0.45 mL ethanol with 50 μL Nafion solution (5 wt.%) to form homogeneous ink assisted by ultrasound. Then 180 μL of the ink was spread onto the surface of carbon cloth by a micropipette and dried under room temperature. The final loading for all catalysts and 20 % commercial Pt/C electrocatalys on work electrode is 2.4 mg/cm^2 . Experiments were conducted in an 1.0 M KOH electrolyte at room temperature. The potential range was from 2.0 to -1.5 V (vs. Ag/AgCl) and the scan rate was $3 \text{ mV}\cdot\text{s}^{-1}$. Cyclic voltammetry (CV) was carried out to calculate the capacitance (C_{dl}). The obtained C_{dl} can be converted into an electrochemically active surface area (ECSA) using the formula: $\text{ECSA} = \frac{C_{dl}}{C_s}$, where the specific capacitance value (C_s)

was $40 \mu\text{F}\cdot\text{cm}^{-2}$.^[1] All the polarization curves were recorded with a 90% iR compensation. As for the Faradaic efficiency measurements, gas chromatography (Agilent 6820, Ar carrier, molecule sieve 5A column, TCD detector) was used to determine the experimentally evolved amount of H_2 and O_2 . Faraday law to calculate the theoretical amount of H_2 and O_2 expected based on a chronoamperometry.

Characterization.

Solution ^1H NMR experiments were performed on a Bruker DMX 300 NMR spectrometer (300 MHz) with d_6 -dimethyl sulfoxide as the standard. The chemical shift data were later processed by the MestReNova Program. Differential scanning calorimetry (DSC) was performed using a Q2000 DSC (TA Instruments-Waters LLC, USA) system at a heating rate of $10 \text{ }^\circ\text{C}\cdot\text{min}^{-1}$. XRD patterns were collected using a Rigaku D/max-2500 diffractometer. AFM was taken on a Bruker Multimode 8 instrument under the AC mode (tapping mode). Sample morphologies were characterized using a Hitachi SU8010 field emission scanning electron microscope (FESEM) and JEOL-2100F TEM. X-ray photoelectron spectroscopic (XPS) analysis was performed by an ESCALAB MK X-ray photoelectron spectrometer. The spectra were calibrated using the C1s (284.8 eV). We fit peaks by means of XPS-peak-differenating analysis software called "XPSPEAK4.0". FT-IR spectra were recorded on Bruker Tensor 27 IR spectrometer

and the sample was prepared by the KBr pellet method. Specific surface areas and pore size distribution were analyzed on Micromeritics ASAP 2020 N₂ adsorption analyzer using the BET (Brunauer-Emmet-Teller) and BJH (Barrett-Joyner-Halenda) methods, respectively.

Density functional theory (DFT) calculation.

The DFT calculations were conducted using the Dmol3 code^[2] with DN basis to express the wave function of valence electrons and DFT Semi-core Pseudopotentials (DSPPs) to describe the interactions of valence electrons and ionic cores. The functional of generalized gradient approximation (GGA) with Perdew, Burke, and Ernzerhof (PBE)^[3] was used throughout to describe the electron-electron exchange and correlation interactions. For the sampling of Brillouin-zone integrals, a (1×1×1) k-point grid was used, and meanwhile, global Orbital cutoff 4.5 Å was employed as the maximum value from all the cutoffs specific to each element in this system. The convergence tolerance of an energy of 10⁻⁵ Ha was taken, and the relaxation of the unit cell, including the atoms, was performed by Geometry Optimization. The atom positions were relaxed until the remaining force acting on the atoms was less than 4 × 10⁻⁴ Ha Å⁻¹.

Turn-over frequency analysis.

The total number of hydrogen turnovers was calculated from the current density according to:

$$\begin{aligned} \# H_2 &= (j) \left(\frac{1 C \cdot S^{-1}}{1000 mA} \right) \left(\frac{1 mol \cdot e^{-}}{96485.3 C} \right) \left(\frac{1 mol H_2}{2 mol e^{-}} \right) \left(\frac{6.022 \times 10^{23} H_2 \text{ molecules}}{1 mol H_2} \right) \\ &= 3.12 \times 10^{15} \frac{H_2 / s}{cm^2} \frac{mA}{cm^2} \text{ per } \frac{mA}{cm^2} \end{aligned}$$

The active sites per real surface are calculated from the following formula:

The hexagonal unit cell has a molar volume of Ni₂P:

$$V_m = \frac{M}{\rho} = \frac{148.37 g \cdot mol^{-1}}{7.351 g \cdot cm^{-3}} = 20.184 \frac{cm^3}{mol \cdot Ni_2P}$$

Each formula unit contains 3 atoms of Ni and P.

The average surface occupancy thus becomes:

$$\text{Number of active sites (Ni}_2\text{P)} = \left(\frac{3 \text{ atoms / formula unit}}{20.184 \text{ cm}^3/\text{mol Ni}_2\text{P}} \right)^{2/3} = 2.0 \times 10^{15} \text{ atoms/cm}^2$$

$$\frac{6.022 \times 10^{23} \text{ mol}^{-1}}$$

Finally, plot of current density can be converted into a TOF according to:

$$\text{TOF} = \frac{(3.12 \times 10^{15} \frac{\text{H}_2/\text{s}}{\text{cm}^2} \text{ per } \frac{\text{mA}}{\text{cm}^2}) \times |j|}{\# \text{ active sites} \times A_{\text{ECSA}}}$$

2. Supplementary Figures and Discussion

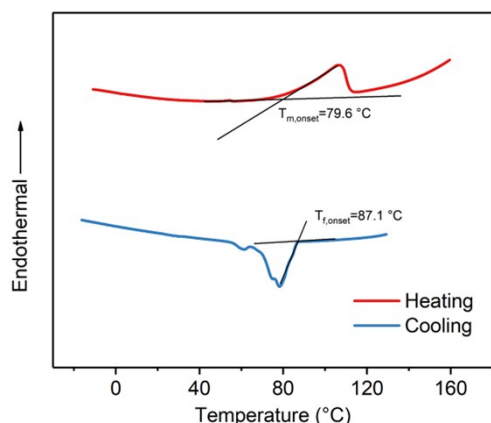


Figure S1. Differential Scanning Calorimeter (DSC) spectra of DES-3.

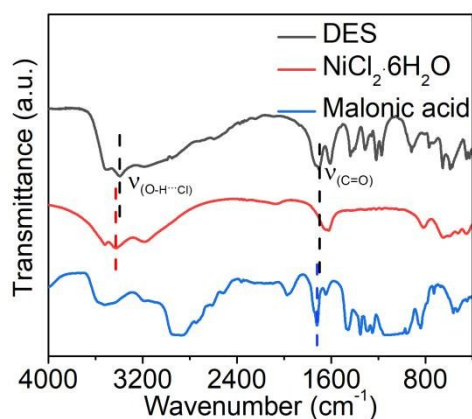


Figure S2. FT-IR spectra of DES-3, $\text{NiCl}_2 \cdot 6\text{H}_2\text{O}$, and malonic acid.

In order to characterize the mixture solvents, differential scanning calorimetry (DSC) and infrared (IR) spectra were carried out. It can be confirmed from the DSC curves that DES ($n_{\text{NiCl}_2 \cdot \text{H}_2\text{O}} : n_{\text{malonic acid}} = 1:7$) starts to melt from 79.6 °C, and the melting point of other DESs with different molar ratio are listed in Table S1. As can be seen that with the molar ratio of malonic acid increases, the melting point of DES first decreases and then increases, the detail melting point as shown in Table S1. This eutectic temperature is lower than the melting point of malonic acid (135 °C) and $\text{NiCl}_2 \cdot 6\text{H}_2\text{O}$ (140 °C) (Figure S1). In addition, infrared (IR) spectroscopy confirms the interaction between the components that compose DES (Figure S2). Before the formation of DES, in $\text{NiCl}_2 \cdot 6\text{H}_2\text{O}$, hydroxyl group of water interacted with chloride, whose vibration mode was $\text{O-H} \cdots \text{Cl}$. The O-H corresponded to peak around 3428.5 cm^{-1} . After the formation of DES, chloride and carboxyl group of malonic acid formed a new vibration mode, $\text{O-H} \cdots \text{Cl}$. This weakens the original vibration mode. And, as a result, the above peak moves toward low wave numbers. Similarly, in pure malonic acid, the stretching vibration peak of the

carbonyl group is 1718.0 cm^{-1} , and after forming DES, the peak shifts to 1702.3 cm^{-1} . This is because Ni coordinates with carbonyl oxygen. The above interactions are beneficial for the formation of DESs. DSC demonstrated the formation of DES; the interactions between hydrogen bond donors and acceptors verified the intrinsic cause of the formation of DESs.

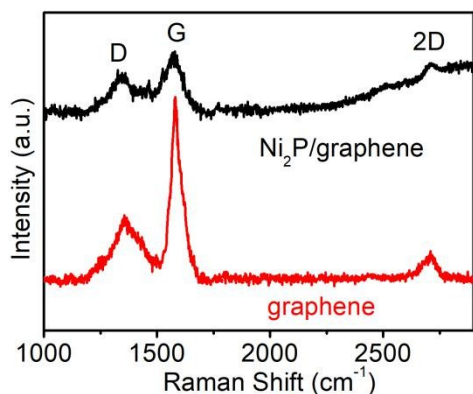


Figure S3. Raman spectra of Ni_2P and $\text{Ni}_2\text{P}@$ graphene.

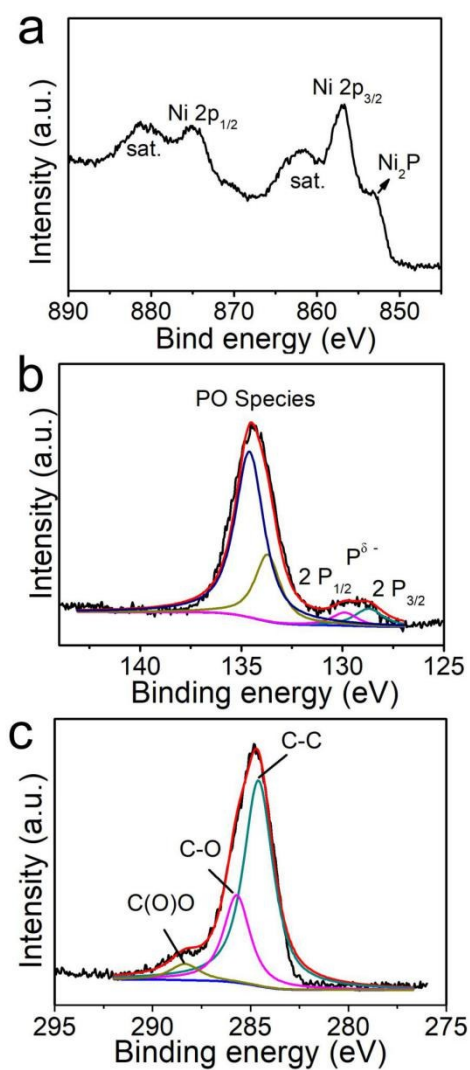


Figure S4. XPS studies of the catalysts for (a) Ni 2p, (b) P 2p, and (d) C 1s.

X-ray photoelectron spectroscopy (XPS) measurements were performed to analyze the surface electronic state and composition of Ni₂P/G. The presence of elements C, Ni, and P has been supported by the survey scan spectrum (Fig. S4). For the C 1s XPS spectrum of the nanohybrid, signals including the aromatic linked carbon (C=C, 284.6 eV), the C in oxygen single-bonded carbon bonds (C-O, 285.7 eV), and the carboxylate carbon (O-C=O, 288.4 eV) can be observed (Fig. S4c), indicating that there are oxygen-containing functional groups on the graphene shell.^[4] These functional groups are highly active for anchoring Ni-P species during the synthesis process, thus greatly enhancing the structural stability of the nanohybrids.^[5, 6] Fig. S4b shows the high resolution spectrum of Ni 2p, the peak of the binding energy of 852.9 eV (Ni 2p_{3/2}) is consistent with the Ni^{δ+} of Ni₂P.^[7] The binding energy of 873.7 and 856.1 eV and the corresponding two satellite peaks are attributed to Ni 2p_{3/2} and Ni 2p_{1/2} in the nickel oxide produced by the surface oxidation of Ni₂P. The corresponding P 2p edge confirmed the presence of P^{δ-} at 129 eV.^[8, 9]

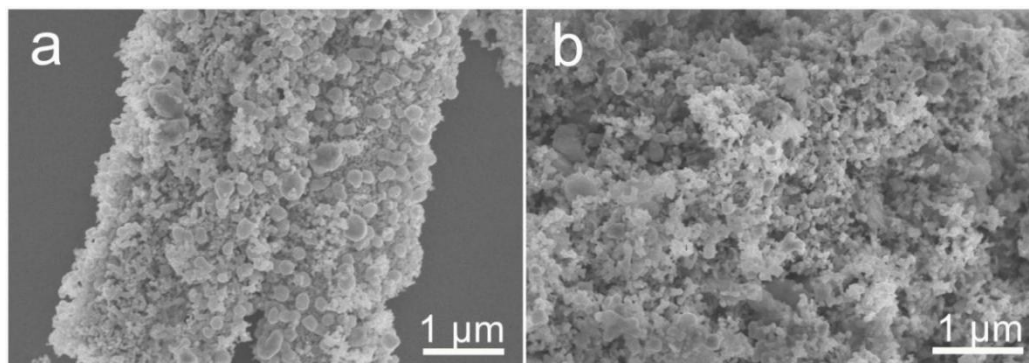


Figure S5. SEM images of Ni₂P@G prepared at different pyrolysis temperatures, a) 300 °C, b) 500 °C.

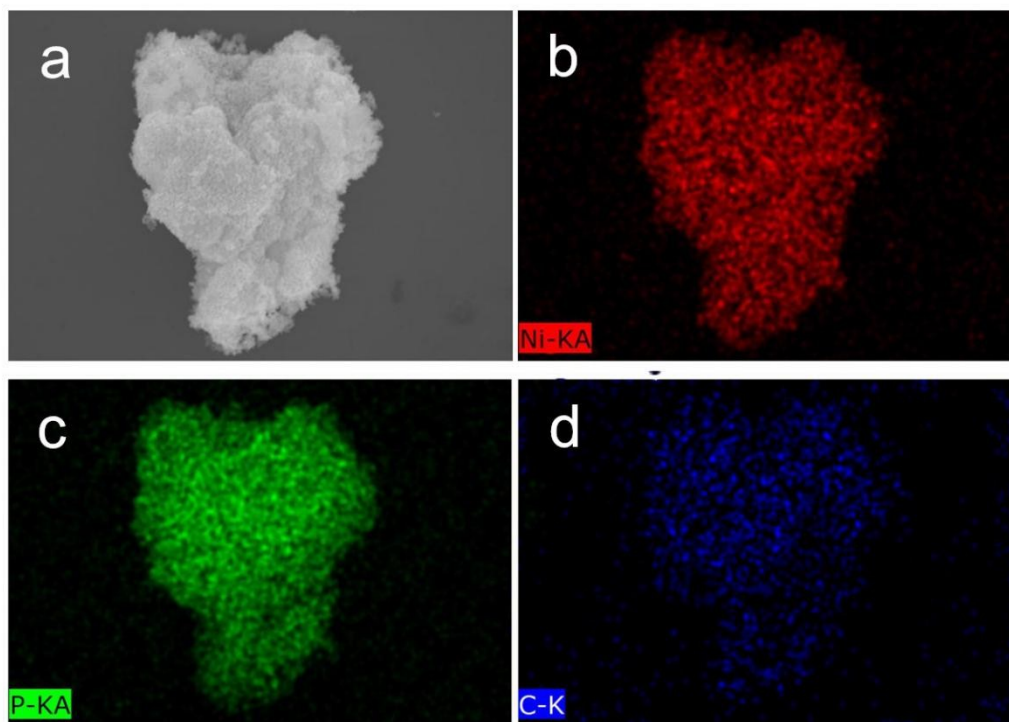


Figure S6. SEM and the corresponding elemental mapping of $\text{Ni}_2\text{P}@G-3$.

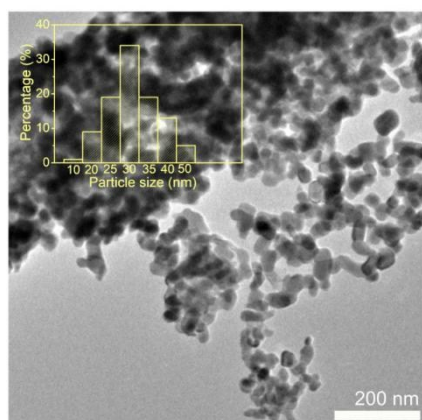


Figure S7. TEM image of $\text{Ni}_2\text{P}@G-3$. Inset: particle size distribution of the samples.

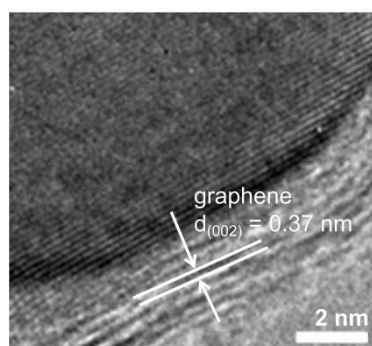


Figure S8. HRTEM images of $\text{Ni}_2\text{P}@G-3$ composites.

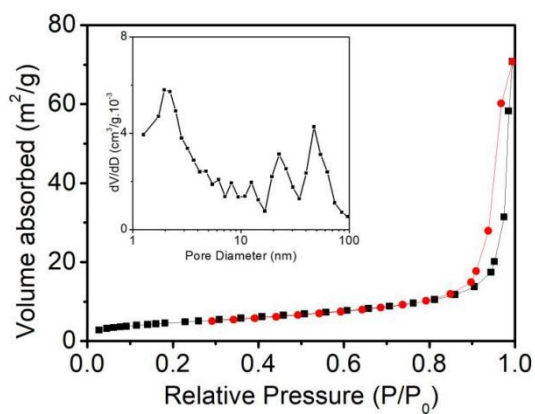


Figure S9. N_2 adsorption-desorption isotherms of $\text{Ni}_2\text{P}@$ graphene and the corresponding pore-size distribution plots (insert image).

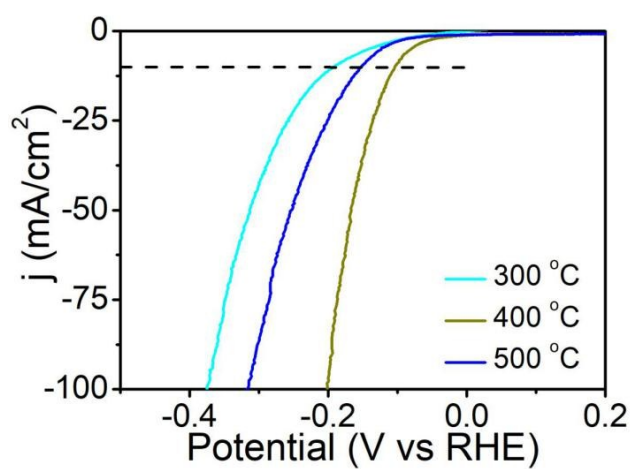


Figure S10. LSV curves of $\text{Ni}_2\text{P}@$ G prepared at different pyrolysis temperatures.

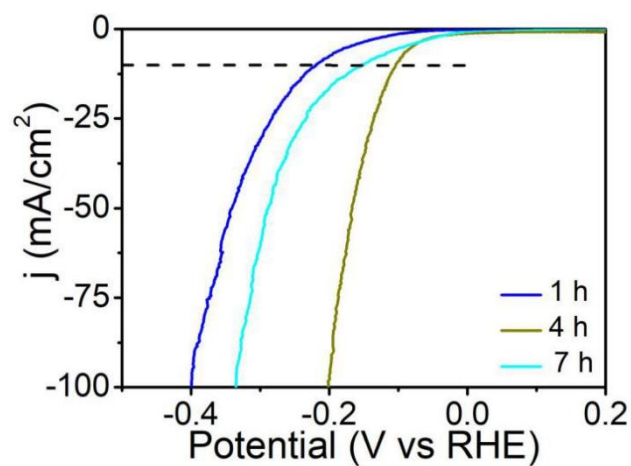


Figure S11. LSV curves of $\text{Ni}_2\text{P}@$ G prepared at different pyrolysis times.

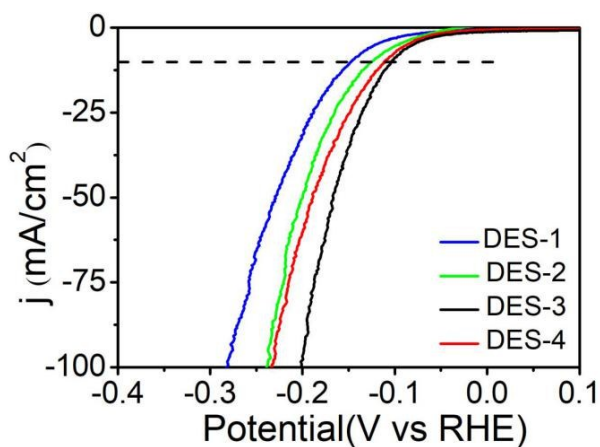


Figure S12. LSV curves of Ni₂P@G with different molar ratios of NiCl₂·6H₂O and malonic acid.

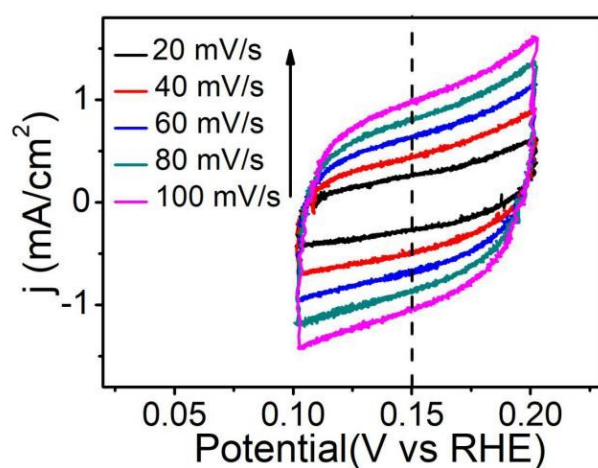


Figure S13. Cyclic voltammetry of Ni₂P@G-3 0.10-0.2 V (vs. RHE) at different scan rate.

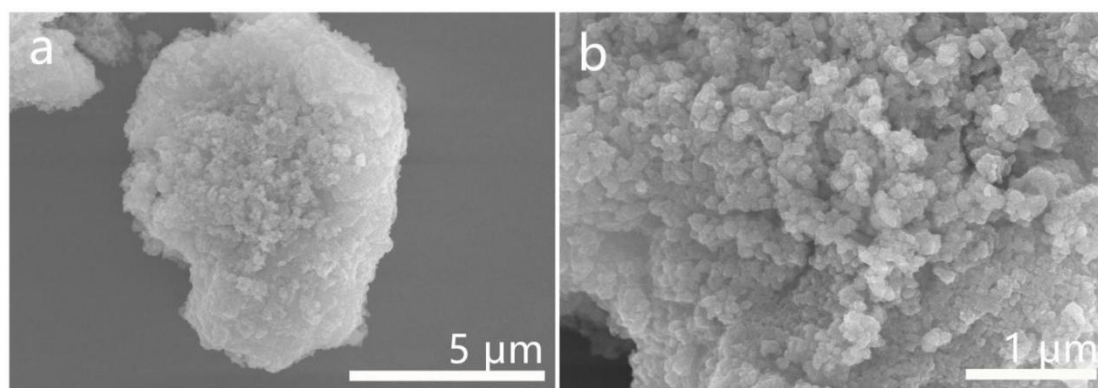


Figure S14. SEM images of Ni₂P@G-3 after stability experiments.

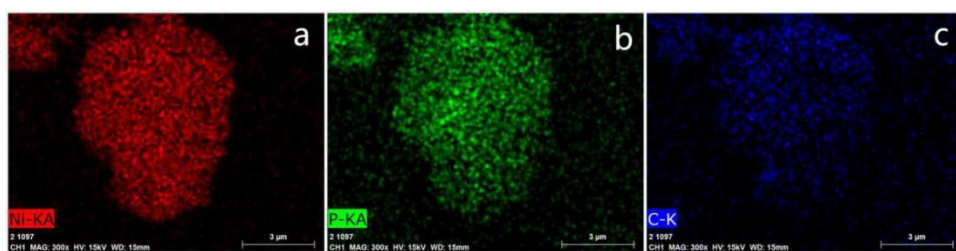


Figure S15. Elemental mapping of Ni₂P@G-3 after stability experiments.

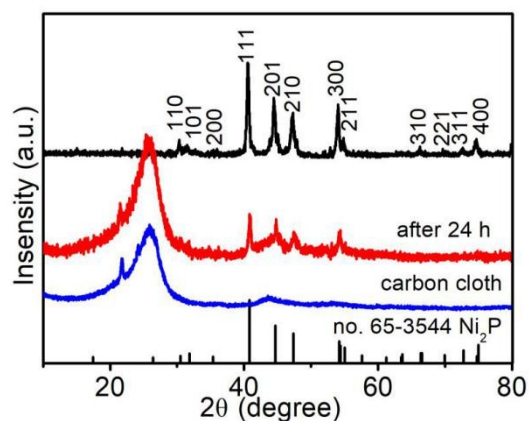


Figure S16. XRD patterns of initial and after stability experiments of Ni₂P@G-3, and carbon cloth.

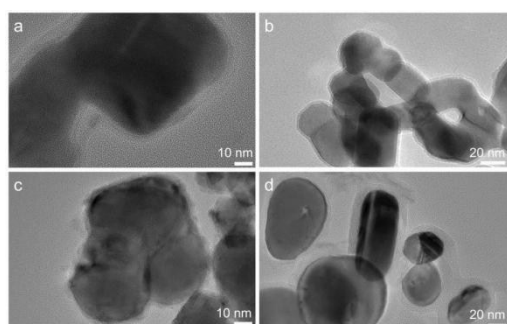


Figure S17. TEM images of Ni₂P@G prepared at different graphene precursors. (a) oxalic acid, (b) malonic acid, (c) succinic acid, and d) glutaric acid)

It can be seen from TEM images that graphene encapsulated Ni₂P composites can be prepared with different carboxylic acid precursors.

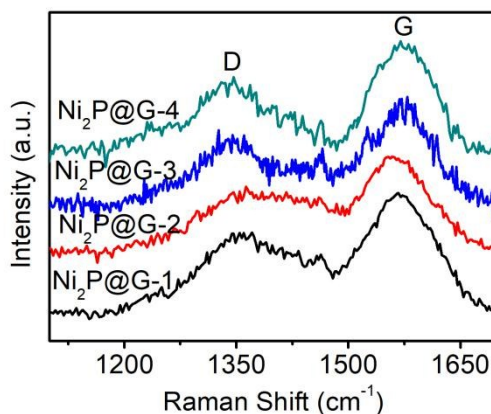


Figure S18. Raman spectra of Ni₂P@G-1, Ni₂P@G-2, Ni₂P@G-3, and Ni₂P@G-4.

According to the Raman spectra, the intensity ratio of 1D/1G of graphene ranged from 0.627 to 0.648, this indicated that the graphene in Ni₂P@G prepared by NiCl₂·6H₂O and malonic acid with different molar ratio had the same defects and degree of graphitization.

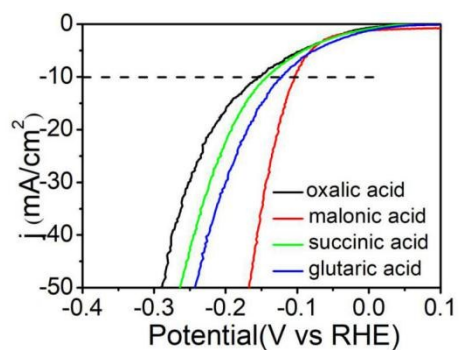


Figure S19. LSV curves of products obtained from different carboxylic acid precursors.

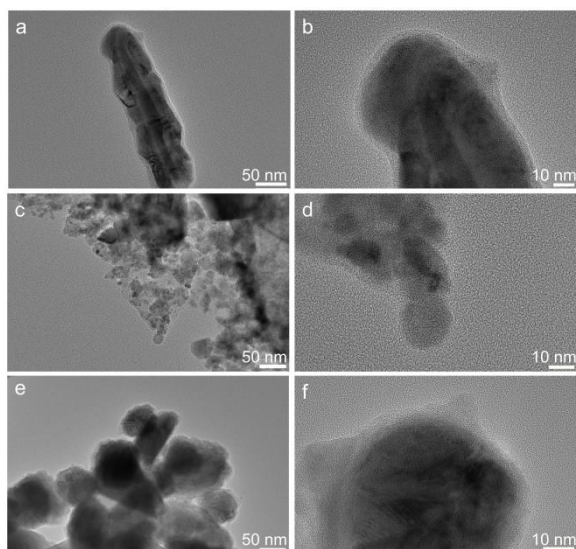


Figure S20. TEM images of a) copper phosphide@G, c) iron phosphide@G, and e) cobalt phosphides; HRTEM images of b) copper phosphide@G, d) iron phosphide@G, and f) cobalt phosphides.

The TEM and HRTEM images of the synthesis of different metal phosphatides by malonic acid and metal chloride are shown in Figure S19. As can be seen from TEM and HRTEM images, the synthesized metal phosphatides are all coated with graphite.

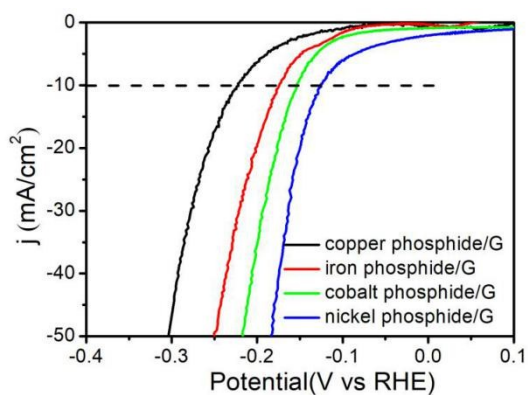


Figure S21. LSV curves of different phosphatides.

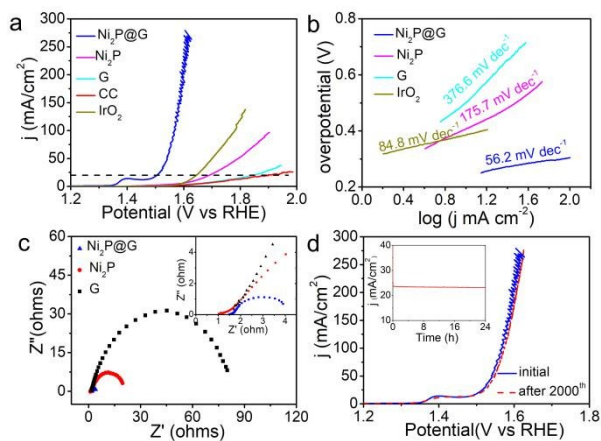


Figure S22. (a) OER linear sweeping voltammetry curves of $\text{Ni}_2\text{P@G-3}$, Ni_2P , G, IrO_2 , and CC electrodes. Corresponding (b) Tafel plots. (c) Nyquist plots (at $\eta = 300$ mV). (d) Stability of $\text{Ni}_2\text{P@G-3}$ with an initial polarization curve and after 2000 cycles (the inset image shows chronoamperometric curve).

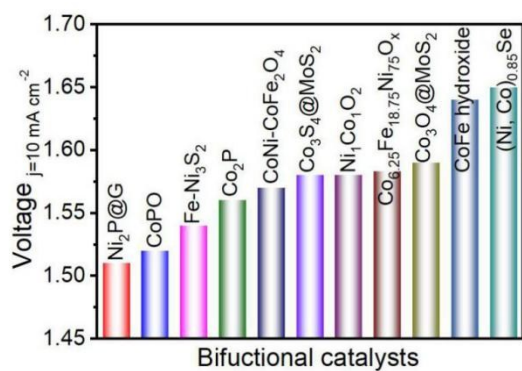


Figure S23. Comparison of voltage between $\text{Ni}_2\text{P@G}$ and other state-of-the-art non-precious metal dual-function catalysts at $10 \text{ mA} \cdot \text{cm}^{-2}$ current density^[10-19]

3. Supplementary Tables

Table S1. The freezing point of DES-1, DES-2, DES-3, and DES-4.

	DES-1	DES-2	DES-3	DES-4
melting point (°C)	76.2	54.8	54.6	59.4

Table S2. Compare the HER performance of Ni₂P@G with other reported non-precious HER electrocatalysts.

Catalysts	η_{10} (mV)	Tafe Slope (mV dec ⁻¹)	electrolyte	Ref.
Ni ₂ P@G	103	56.5	1M KOH	this work
Zn-Co-S	176	86.3	1M KOH	20
NiO	110	100	1M KOH	21
MoSe ₂ -CoSe ₂	237	89	1M KOH	22
Mo ₂ N-Mo ₂ C	154	68	1M KOH	23
Fe _{1.89} Mo _{4.11} O ₇ -MoO ₂	197	79	1M KOH	24
Cu-Ni ₃ S ₂	128	76.2	1M KOH	25
Co _x Mo _y @N-carbon	218	73.5	1M KOH	26
C, N doped carbon	380	76.9	1M KOH	27
1T-MoSe ₂	152	52	0.5 M H ₂ SO ₄	28
carbon nanotubes-MoSe ₂	170	67	0.5 M H ₂ SO ₄	29
Fe _{4.5} Ni _{4.5} S ₈	146	--	0.5 M H ₂ SO ₄	30
Fe-MoS ₂	104	59	0.5 M H ₂ SO ₄	31
Mo ₂ C	229	100.7	0.5 M H ₂ SO ₄	32
Monolayer MoS ₂	385	109	0.5 M H ₂ SO ₄	33
N@MoPC _x	108	69.4	0.5 M H ₂ SO ₄	34

Table S3. Compare the OER performance of Ni₂P@G with other reported non-precious OER electrocatalysts in KOH electrolyte.

Catalysts	η_{10} (mV)	Tafe Slope (mV dec ⁻¹)	Ref.
Ni ₂ P@G	η_{20} =275	56.2	this work
NiCo@NiCoO ₂	η_{20} =366	83.97	35
CeO ₂ -embedded NiO	382	118.7	36
Co _{0.708} Fe _{0.29} 2WO ₄	327	53	37
Co ₃ O ₄	307	56	38
Co ₉ S ₈ @carbon	302	67	39
CoOOH	266	30	40
CoO _x	306	67	41
MoS ₂	370	39	42
N-CoFe LDHs	281	40.03	43
Ni _{0.6} Co _{1.4} P	300	80	44
Ni _{0.13} Co _{0.87} S _{1.097}	316	54.72	45
NiCoP	297	57.35	46
Ni-Fe LDH	280	49.4	47
NiPS ₃	301	43	48
SnCoFe-Ar	300	42.3	49

4. References

- [1] C. McCrory, S. Jung, J. C. Peters, T. F. Jaramillo, *J. Am. Chem. Soc.*, 2013, **135**, 16977.
- [2] J. P. Perdew, K. Burke, M. Ernzerhof, *Phys. Rev. Lett.*, 1996, **77**, 3865.
- [3] B. Delley, *J. Chem. Phys.*, 2000, **113**, 7756.
- [4] L. Wang, T. Wei, L. Z. Sheng, L. Jiang, X. L. Wu, Q. H. Zhou, B. Yuan, J. M. Yue, Z. Liu, Z. J. Fan, *Nano energy*, 2016, **30**, 84.
- [5] P. Chen, T. Y. Xiao, Y. H. Qian, S. S. Li, S. H. Yu, *Adv. Mater.*, 2013, **25**, 3192.
- [6] S. Chen, S. Z. Qiao, *ACS Nano*, 2013, **7**, 10190.
- [7] S. F. Fu, C. Z. Zhu, J. H. Song, M. H. Engelhard, X. Li, D. Du, Y. H. Lin, *ACS Energy Lett.*, 2016, **4**, 792.
- [8] L. A. Stern, L. Q. Feng, F. Song, X. L. Hu, *Energy Environ. Sci.*, 2015, **8**, 2347.
- [9] M. Ledendecker, S. Krick Calderón, C. Papp, H. P. Steinrück, M. Antonietti, M. Shalom, *Angew. Chem. Int. Ed.*, 2015, **54**, 12361.
- [10] G. Anandhababu, Y. Huang, D. D. Babu, M. X. Wu, Y. B. Wang, *Adv. Funct. Mater.*, 2018, **28**, 1706120.
- [11] G. Zhang, Y. S. Feng, W. T. Lu, D. He, C. Y. Wang, Y. K. Li, F. F. Cao, *ACS Catal.*, 2018, **8**, 5431.
- [12] H. Li, Q. Li, P. Wen, T. B. Williams, S. Adhikari, C. C. Dun, C. Lu, D. Itanze, L. Jiang, D. Carroll, G. Donati, P. Lundin, Y. J. Qiu, S. Geyer, *Adv. Mater.*, 2018, **30**, 1705796.
- [13] G. Zhang, Y. S. Feng, W. T. Lu, D. He, C. Y. Wang, Y. K. Li, X. Y. Wang, F. F. Cao, *ACS Catal.*, 2018, **8**, 5431.
- [14] Y. N. Guo, J. Tang, H. Y. Qian, Z. L. Wang, Y. Yamauchi, *Chem. Mater.*, 2017, **29**, 5566.
- [15] H. Xu, J. J. Wei, M. Zhang, J. Wang, Y. Shiraishi, L. Tian, Y. Du, *Nanoscale*, 2018, **10**, 18767.
- [16] Z. C. Wu, X. Wang, J. S. Huang, F. Gao, *J. Mater. Chem. A*, 2018, **6**, 167.
- [17] J. Liu, J. S. Wang, B. Zhang, Y. J. Ruan, H. Z. Wan, X. Ji, K. Xu, D. Zha, L. Miao, J. Jiang, *J. Mater. Chem. A*, 2018, **6**, 2067.

- [18] P. Babar, A. Lokhande, H. H. Shin, B. Pawar, M. G. Gang, S. Pawar, J. H. Kim, *Small*, 2018, **14**, 1702568.
- [19] K. M. Xiao, L. Zhou, M. Shao, M. F. Wei, *J. Mater. Chem. A*, 2018, **6**, 7585.
- [20] B. W. Zhang, G. Yang, C. J. Li, K. Huang, J. S. Wu, S. J. Hao, J. Y. Feng, D. D. Peng, Y. Z. Huang, *Nanoscale*, 2018, **10**, 1774.
- [21] T. Zhang, M. Y. Wu, D. Y. Yan, J. Mao, H. Liu, W. B. Hu, X. W. Du, T. Ling, S. Z. Qiao, *Nano Energy*, 2018, **43**, 103.
- [22] X. Q. Wang, B. J. Zheng, B. Yu, B. Wang, W. Q. Hou, W. L. Zhang, Y. F. Chen, *J. Mater. Chem. A*, 2018, **6**, 7842.
- [23] H. J. Yan, Y. Xie, Y. Q. Jiao, A. P. Wu, C. G. Tian, X. M. Zhang, L. Wang, H. G. Fu, *Adv. Mater.*, 2018, **30**, 1704156.
- [24] Z. M. Hao, S. S. Yang, J. Y. Niu, Z. Q. Fang, L. L. Liu, Q. S. Dong, S. Y. Song, Y. Zhao, *Chem. Sci.*, 2018, **9**, 5640.
- [25] J. X. Feng, J. Q. Wu, Y. X. Tong, G. R. Li, *J. Am. Chem. Soc.*, 2018, **140**, 610.
- [26] J. Jiang, Q. X. Liu, C. M. Zeng, L. H. Ai, *J. Mater. Chem. A*, 2017, **5**, 16929.
- [27] K. G. Qu, Y. Zheng, X. X. Zhang, K. Davey, S. Dai, S. Z. Qiao, *ACS nano*, 2017, **11**, 7293.
- [28] Y. Yin, Y. M. Zhang, T. L. Gao, T. Yao, X. H. Zhang, J. C. Han, X. J. Wang, Z. H. Zhang, P. Xu, P. Zhang, X. Z. Cao, B. Song, S. Jin, *Adv. Mater.*, 2017, **29**, 1700311.
- [29] L. Najafi, S. Bellani, R. Oropesa-Nuñez, A. Ansaldo, M. Prato, A. E. Del Rio Castillo, F. Bonaccorso, *Adv. Energy Mater.*, 2018, **8**, 1703212.
- [30] S. Piontek, C. Andronescu, A. Zaichenko, B. Konkona, K. Junge Puring, B. Marler, H. Antoni, I. Sinev, M. Muhler, D. Mollenhauer, B. R. Cuenya, W. Schuhmann, U. Apfel, *ACS Catal.*, 2018, **8**, 987.
- [31] J. Hu, B. L. Huang, C. X. Zhang, Z. L. Wang, Y. M. An, D. Zhou, H. Lin, M. K. H. Leung, S. H. Yang, *Energy Environ. Sci.*, 2017, **10**, 593.
- [32] J. S. Kang, J. Kim, M. J. Lee, Y. J. Son, D. Y. Chung, S. Park, J. Jeong, J. M. Yoo, H. Shin, H. Choe, H. S. Park, Y. E. Sung, *Adv. Sci.*, 2018, **5**, 1700601.
- [33] S. Q. Su, Qi. W. Zhou, Z. Q. Zeng, D. Hu, X. Wang, M. L. Jin, X. S. Gao, R. Nötzel, G. F. Zhou, Z. Zhang, J. M. Liu, *ACS Appl. Mater. Interfaces*, 2018, **10**, 8026.

- [34] Y. C. Huang, J. X. Ge, J. Hu, J. W. Zhang, J. Hao, Y. G. Wei, *Adv. Energy Mater.*, 2018, **8**, 1701601.
- [35] H. Xu, Z. X. Shi, Y. X. Tong, G. R. Li, *Adv. Mater.*, 2018, **30**, 1705442.
- [36] W. Gao, Z. M. Xia, F. X. Cao, J. C. Ho, Z. Jiang, Y. Q. Qu, *Adv. Funct. Mater.*, 2018, **28**, 1706056.
- [37] W. Shao, Y. H. Xia, X. Luo, L. F. Bai, J. Zhang, G. G. Sun, C. M. Xie, X. D. Zhang, W. S. Yan, Y. Xie, *Nano Energy*, 2018, **50**, 717.
- [38] Y. Li, F. M. Li, X. Y. Meng, S. N. Li, J. H. Zeng, Y. Chen, *ACS Catal.*, 2018, **8**, 1913.
- [39] Z. Chen, R. B. Wu, M. Liu, Y. Liu, S. Y. Xu, Y. Ha, Y. H. Guo, X. B. Yu, D. L. Sun, F. Fang, *J. Mater. Chem. A*, 2018, **6**, 10304.
- [40] S. H. Ye, Z. X. Shi, J. X. Feng, Y. X. Tong, G. R. Li, *Angew. Chem. Int. Ed.*, 2018, **57**, 2672.
- [41] W. J. Xu, F. L. Lyu, Y. C. Bai, A. Q. Gao, J. Feng, Z. X. Cai, Y. D. Yin, *Nano Energy*, 2018, **43**, 110.
- [42] B. Mohanty, M. Ghorbani-Asl, S. Kretschmer, A. Ghosh, P. Guha, S. K. Panda, B. Jena, Ar. V. Krashennnikov, B. K. Jena, *ACS Catal.*, 2018, **8**, 1683.
- [43] Y. Y. Wang, C. Xie, Z. Y. Zhang, D. D. Liu, R. Chen, S. Y. Wang, *Adv. Funct. Mater.*, 2018, **28**, 1703363.
- [44] B. C. Qiu, L. J. Cai, Y. Wang, Z. Y. Lin, Y. P. Zuo, M. Y. Wang, Y. Chai, *Adv. Funct. Mater.*, 2018, **28**, 1706008.
- [45] J. C. Zhang, D. J. Zhang, R. C. Zhang, N. N. Zhang, C. C. Cui, J. R. Zhang, B. Jiang, B. Q. Yuan, T. Y. Wang, H. Xie, Q. Li, *ACS Appl. Energy Mater.*, 2018, **1**, 495.
- [46] Y. J. Zhao, G. L. Fan, L. Yang, Y. J. Lin, F. Li, *Nanoscale*, 2018, **10**, 13555.
- [47] L. Yu, J. F. Yang, B. Y. Guan, Y. Lu, X. W. Lou, *Angew. Chem. Int. Ed.*, 2018, **130**, 178.
- [48] R. Dangol, Z. Dai, A. Chaturvedi, Y. Zheng, Y. Zhang, K. N. Dinh, B. Li, Y. Zong, Q. Y. Yan, *Nanoscale*, 2018, **10**, 4890.
- [49] D. W. Chen, M. Qiao, Y. R. Lu, L. Hao, D. D. Liu, C. L. Dong, Y. F. Li, S. Y. Wang, *Angew. Chem. Int. Ed.*, 2018, **57**, 8691.